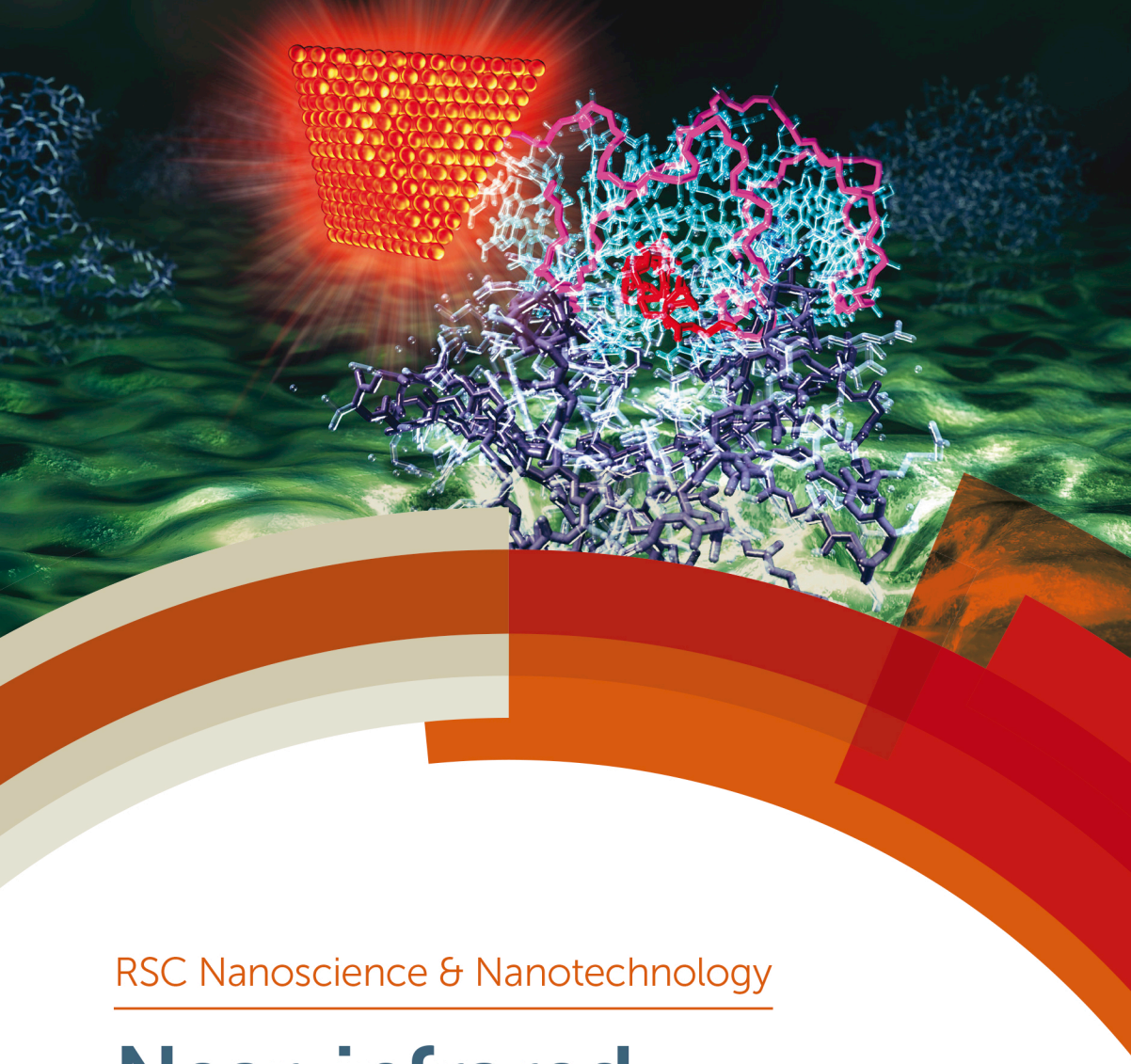

RSC Nanoscience & Nanotechnology

Near-infrared Nanomaterials

Preparation, Bioimaging and Therapy Applications

Edited by Fan Zhang

ROYAL SOCIETY OF CHEMISTRY

Near-infrared Nanomaterials

Preparation, Bioimaging and Therapy Applications

RSC Nanoscience & Nanotechnology

Titles in the Series:

1: Nanotubes and Nanowires
2: Fullerenes: Principles and Applications
3: Nanocharacterisation
4: Atom Resolved Surface Reactions: Nanocatalysis
5: Biomimetic Nanoceramics in Clinical Use: From Materials to Applications
6: Nanofluidics: Nanoscience and Nanotechnology
7: Bionanodesign: Following Nature's Touch
8: Nano-Society: Pushing the Boundaries of Technology
9: Polymer-based Nanostructures: Medical Applications
10: Metallic and Molecular Interactions in Nanometer Layers, Pores and Particles: New Findings at the Yoctolitre Level
11: Nanocasting: A Versatile Strategy for Creating Nanostructured Porous Materials
12: Titanate and Titania Nanotubes: Synthesis, Properties and Applications
13: Raman Spectroscopy, Fullerenes and Nanotechnology
14: Nanotechnologies in Food
15: Unravelling Single Cell Genomics: Micro and Nanotools
16: Polymer Nanocomposites by Emulsion and Suspension
17: Phage Nanobiotechnology
18: Nanotubes and Nanowires, 2nd Edition
19: Nanostructured Catalysts: Transition Metal Oxides
20: Fullerenes: Principles and Applications, 2nd Edition
21: Biological Interactions with Surface Charge Biomaterials
22: Nanoporous Gold: From an Ancient Technology to a High-Tech Material
23: Nanoparticles in Anti-Microbial Materials: Use and Characterisation
24: Manipulation of Nanoscale Materials: An Introduction to Nanoarchitectonics
25: Towards Efficient Designing of Safe Nanomaterials: Innovative Merge of Computational Approaches and Experimental Techniques
26: Polymer–Graphene Nanocomposites

27: Carbon Nanotube-Polymer Composites
28: Nanoscience for the Conservation of Works of Art
29: Polymer Nanofibers: Building Blocks for Nanotechnology
30: Artificial Cilia
31: Nanodiamond
32: Nanofabrication and its Application in Renewable Energy
33: Semiconductor Quantum Dots: Organometallic and Inorganic Synthesis
34: Soft Nanoparticles for Biomedical Applications
35: Hierarchical Nanostructures for Energy Devices
36: Microfluidics for Medical Applications
37: Nanocharacterisation, 2nd Edition
38: Thermometry at the Nanoscale: Techniques and Selected Applications
39: Nanoceramics in Clinical Use: From Materials to Applications, 2nd Edition
40: Near-infrared Nanomaterials: Preparation, Bioimaging and Therapy Applications

How to obtain future titles on publication:
A standing order plan is available for this series. A standing order will bring delivery of each new volume immediately on publication.

For further information please contact:
Book Sales Department, Royal Society of Chemistry, Thomas Graham House, Science Park, Milton Road, Cambridge, CB4 0WF, UK
Telephone: +44 (0)1223 420066, Fax: +44 (0)1223 420247
Email: booksales@rsc.org
Visit our website at www.rsc.org/books

Near Infrared Nanomaterials
Preparation, Bioimaging, and Therapy Applications

Edited by

Fan Zhang
Fudan University, Shanghai, China
Email: zhang_fan@fudan.edu.cn

ROYAL SOCIETY OF CHEMISTRY

THE QUEEN'S AWARDS FOR ENTERPRISE: INTERNATIONAL TRADE 2013

RSC Nanoscience & Nanotechnology No. 40

Print ISBN: 978-1-78262-319-9
PDF eISBN: 978-1-78262-393-9
EPUB eISBN: 978-1-78262-831-6
ISSN: 1757-7136

A catalogue record for this book is available from the British Library

Published by The Royal Society of Chemistry,
Thomas Graham House, Science Park, Milton Road,
Cambridge CB4 0WF, UK

Registered Charity Number 207890

For further information see our web site at www.rsc.org

Printed in the United Kingdom by CPI Group (UK) Ltd, Croydon, CR0 4YY, UK

Foreword

In the last decade, bioimaging and therapy based on near infrared (NIR) nanomaterials have played an important role in biotechnology due to their intrinsic advantages over traditional imaging probes and medicines, such as greater penetration depth, low detection threshold concentration, and better targeted performance. Nanomaterials based on organic dyes, lanthanides, carbon, quantum dots (QDs), and noble metals are major components in this big family of NIR bionanomaterials. Exciting developments have been made at a very fast pace by many research groups. The vast literature published about NIR nanomaterials over the past two decades is a clear witness to this; the number of papers has increased exponentially, with most of the activity and development happening in the last 10 years.

NIR materials have absorption/excitation/emission maxima falling in the region of minimal tissue absorbance/autofluorescence between 650 and 1700 nm, an "imaging window." In tissues, light absorbance and scattering is minimal in this wavelength range, allowing light to penetrate more deeply. This enables animal bioimaging and therapy with high sensitivity in real time without the need for dissection or invasive procedures. In the past two decades, related theories, methods, and techniques have been explored. As a consequence, novel NIR materials are increasingly emerging, and their applications extend from traditional fields such as optical communication amplifiers and solid-state lasers to high-tech fields including biosensors, bioimaging, and disease therapy. Researchers in this field can therefore give a deep insight into synthesis strategies and behavior of NIR nanomaterials, and in particular, establish structure–function–synthesis relationships.

This book contains 11 chapters. Chapter 1 describes some distinctive characteristics of lanthanide-based NIR nanomaterials (upconversion and downconversion) which are directly related to their bioimaging applications,

RSC Nanoscience & Nanotechnology No. 40
Near Infrared Nanomaterials: Preparation, Bioimaging and Therapy Applications
Edited by Fan Zhang

Published by the Royal Society of Chemistry, www.rsc.org

such as color tunability, energy transfer principles, and some strategies for enhancing luminescent efficiency. Bioimaging based on NIR QDs has advantages including lower absorption and relatively low autofluorescence, resulting in deeper penetrating depth and lower background. Chapter 2 summarizes developments in non-toxic QDs, especially for synthesis and *in vivo* bioimaging. Chapter 3 introduces the fabrication and fundamental properties of carbon dots (CDs) and nanodiamonds (NDs) and then focuses on their recent bioapplications in bioimaging. Challenges and perspectives for future developments are also briefly discussed. We hope this chapter will provide critical insights to inspire further exciting research on CDs/NDs for biological imaging applications, to better realize the potential of these intriguing materials in the near future. Chapter 4 summarizes recent progress in the synthesis and *in vivo* behavior of NIR-emitting gold nanoparticles, and discusses future challenges and opportunities for them.

Besides the inorganic NIR nanomaterials already mentioned, nanomaterials based on organic molecules are a novel type of NIR imaging agents. Chapter 5 focuses on recent progress in this area, including major NIR organic chromophores, luminescent principles, and construction methods, as well as biomedical applications and challenges. Photodynamic therapy (PDT) is a treatment for cancer that uses the reactive oxygen species generated by a photosensitizer drug following irradiation at a specific wavelength to destroy cancerous tissue. Chapter 6 provides an overview of the main principles and mechanisms for biosensing based on NIR QDs and the use of QDs for simultaneous diagnostics and therapy of disease. Chapter 7 focuses on state-of-the art use of NIR nanomaterials for PDT, including both *in vitro* and *in vivo* applications. Chapter 8 introduces NIR light-triggered drug and gene delivery platforms, including photoresponsive nanocarriers, photocaging of bioactive cargos, and photothermal transduction for NIR-triggered nanocarriers. It has been suggested that, due to the differences in cell-killing mechanisms, synergetic tumor responses may be achieved if two modalities are combined in an appropriate sequence. Therefore, multifunctional nanocarriers that enable combination cancer therapy with different therapeutic mechanisms in one system may play increasingly important roles in the fight against cancer due to their unique advantages such as minimal side effects and high efficacies. In Chapter 9, we discuss the most significant progress made in the field of NIR-responsive nanotheranostics for synergistic cancer therapy. NIR-induced photothermal ablation therapy (PAT) has attracted increasing interest as a minimally invasive and potentially effective treatment technology for cancer. A prerequisite for the development of NIR-induced PAT is to obtain low-cost and biocompatible photothermal agents with high photothermal conversion efficiency. In Chapter 10, we first introduce the measurement method for photothermal conversion efficiency, and then summarize the research progress of these photothermal agents as well as the combination of PAT with other nanobiotechnology techniques.

Numerous and extensive studies have been devoted to the design, synthesis, and development of various NIR nanomaterials for biomedical imaging

and imaging-guided therapy of cancers; however, so far there is little information on the toxicological properties of NIR nanomaterials and their long-term toxicity or health effects. Moreover, most of the present data are either conflicting or not in the public domain, preventing the scientific community from properly evaluating the effect of nanomaterials on human health and environment. Therefore, Chapter 11 focuses primarily on recent progress in toxicity studies of NIR nanomaterials (including carbon-based materials, QDs, noble metal-based nanoparticles, upconversion nanoparticles, and narrow-bandgap semiconductors), discussing in detail how the biophysicochemical properties of NIR nanomaterials influence their toxicity, and finally presenting a broad overview of the available *in vitro* and *in vivo* toxicity assessments.

Research on NIR nanomaterials has developed rapidly in the past decade. A comprehensive review is thus necessary, and it is the main purpose of this book. Chapters are organized along the following lines: (1) following the forefront of current research, and striving to reflect the latest progress and developments; (2) comprehensive review focusing on basic fundamental research; and (3) practical research experience in methodology, experimental skills, and data analysis. Each chapter also includes understanding, induction, and summaries from the authors. We have taken care to include fundamental information about NIR nanomaterials, making the book especially suitable for beginners and graduate students who have just entered this field. We hope that, through reading this book, they can fully understand the chemistry of photon upconversion nanomaterials, grasp the skills required for their synthesis, obtain high-quality materials, and therefore learn to deeply appreciate the chemical and physical properties of these materials and their applications.

This book is a distillation of the authors' knowledge and hard work. We want it to help and inspire researchers who are working in the fields of chemistry and materials science, especially in nanobiology. We also hope it can provide a reference source or serve as a textbook for undergraduate and graduate students majoring in chemistry, chemical engineering, physics, materials science, and biology, as well as readers who are already interested in NIR nanomaterials.

Galen Stucky
University of California, Santa Barbara

Contents

RSC Nanoscience & Nanotechnology No. 40
Near Infrared Nanomaterials: Preparation, Bioimaging and Therapy Applications
Edited by Fan Zhang

Published by the Royal Society of Chemistry, www.rsc.org

CHAPTER 1

Lanthanide-Based Near Infrared Nanomaterials for Bioimaging

RUI WANG[a] AND FAN ZHANG*[a]

[a]Fudan University, Department of Chemistry, 220 Handan Rd, Shanghai, 200433, P. R. China
*E-mail: zhang_fan@fudan.edu.cn

1.1 Introduction

Lanthanide elements are spectroscopically rich species, a property that facilitates their use as optical codes in a spectral window distinct from fluorescent dyes used for labeling biological samples. The lanthanide 4f orbitals are buried beneath the 6s, 5p, and 5d orbitals; hence, spectra arising from f–f transitions are narrow and insensitive to their environment, unlike transition metal (3d) spectra.[1] Most importantly, this gives rise to a rich energy-level structure in the near infrared (NIR), visible (VIS), and ultraviolet (UV) spectral range (Figure 1.1). Triply ionized lanthanide ions in solid hosts typically have emission line widths of ~10–20 nm (FWHM, full width at half maximum), which is about half that observed for quantum dots (QDs, ~25–40 nm) and much narrower than that observed for organic dyes (~30–50 nm) or transition metal ions (~100 nm).[2,3] This feature allows more resolvable bands to be packed into the same spectral bandwidth, which enables a larger

RSC Nanoscience & Nanotechnology No. 40
Near Infrared Nanomaterials: Preparation, Bioimaging and Therapy Applications
Edited by Fan Zhang

Published by the Royal Society of Chemistry, www.rsc.org

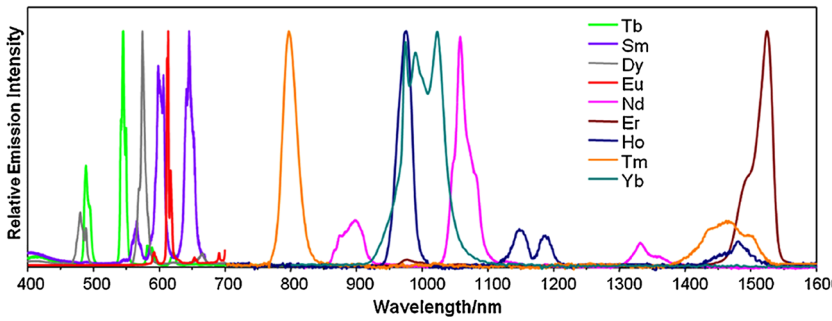

Figure 1.1 Normalized emission spectra of luminescent lanthanide complexes in solution, illustrating the sharp emission bands and minimal overlap of lanthanide luminescence.[4–6] (Reproduced with permission from S. Petoud, *et al.*, *J. Am. Chem. Soc.*, 2003, **125**, 13324–13325.[5] Copyright (2003) American Chemical Society and from ref. 6 with permission from John Wiley and Sons. Copyright © 2005 Wiley-VCH Verlag GmbH & Co. KGaA, Weinheim.)

number of distinct combinations. Because lanthanide emissions involve only atomic transitions, they are extremely resistant to photobleaching. The energy-level structure in lanthanide ions also creates the possibility for large shifts between the excitation and emission bands. This shift can be several hundred nanometers, containing discrete gaps with zero absorption. By comparison, the HOMO–LUMO (highest occupied molecular orbital–lowest unoccupied molecular orbital) transition in organic dyes typically results in overlapping excitation and emission bands and a Stokes shift of only 10–30 nm between the absorption and emission maxima. The large variety of absorption and emission wavelengths, the independence on host materials, and low vibration energy losses make lanthanides ions be ideal for spectral conversion. Lanthanide ions can be doped in a variety of solids such as crystals, fibers, or glass ceramics to give them the desired downconversion and upconversion optical properties. Thus, their remarkable luminescence properties have been widely applied in lasers, solar cells, analytical sensors, photodynamic therapy, and optical imaging.[4–6] In this chapter, we focus on some distinct characteristics of lanthanide-based NIR nanomaterials that are closely related to their bioimaging applications, such as color tunability, energy transfer principles, and some strategies for enhancing luminescent efficiency. In addition, we systematically introduce the most recent bioimaging work based on lanthanide NIR nanomaterials.

1.2 Upconversion Nanoparticles (UCNPs)

Upconversion materials, which emit high-energy photons under excitation by the NIR light (anti-Stokes shift) were first discovered in the 1960s,[7] but have primarily been exploited for the development of some remarkably effective optical devices such as infrared quantum counter detectors,[8,9]

temperature sensors,[10,11] and compact solid state lasers.[12–15] Thus, for more than 30 years the use of the upconversion effect has been limited to bulk glass or crystalline materials.[16–19] Because of their suitable size (small enough to go in and out through many biological host materials, such as the cytoplasm or nucleus of a cell) and their unique properties, such as high chemical stability, low cytotoxicity, and high signal-to-noise ratio, the biological applications of UCNPs for analytical assays and bioimaging were readily recognized.[20–23] The upconversion process proceeds by different mechanisms: excited state absorption (ESA), energy transfer upconversion (ETU), and photon avalanche (PA).[24] ESA and ETU are based on the sequential absorption of two or more photons by metastable, long-lived energy states. In the case of ESA, the ground state activator absorbs at least two photons of suitable energy sequentially. In ETU, activator and neighboring sensitizer both absorb one photon at first, then energy is transferred between sensitizer and activator, resulting in a population of emitting ions in a highly excited state.[25] PA was first reported by Chivian *et al.* in 1979.[26] They found that when Pr^{3+}-doped $LaCl_3$ or $LaBr_3$ crystal is exposed to laser-pump radiation slightly in excess of a certain critical intensity, the fluorescence of Pr^{3+} increases by orders of magnitude.[13,26] PA-induced UC features an unusual pump mechanism that requires a pump intensity above a certain threshold value and always responds slowly to excitation (up to several seconds). The quantum yield (QY) is differs considerably among these three mechanisms: in theory, ESA < ETU < PA, but PA always needs a rather high excitation energy and suffers from slow response to excitation. The QY of ETU is two orders of magnitude higher than that of ESA, making it well understood and widely applied in many fields.[7]

Efficient UCNPs are composed of three components: a host matrix, a sensitizer, and an activator. An ideal host matrix needs to be optically transparent and have low lattice phonon energy, in order to minimize non-radiative losses and maximize radiative emission. $NaYF_4$,[27–29] $NaGdF_4$,[30,31] $NaLuF_4$,[32] LaF_3,[33] and CaF_2,[34] among others, have proven to be ideal candidates. With the development of nanotechnology, several methods have been used to fabricate uniform monodispersed UCNPs with controlled crystalline phases and sizes, including coprecipitation,[35–42] thermal decomposition,[43–47] hydro(solvo)-thermal synthesis,[48–62] sol–gel process,[63–66] and combustion synthesis,[67] which have been reviewed in many papers.[68–72] A proper choice of synthesis method enables the development of UCNPs whose properties match the need for the applications envisioned. On the other hand, the rational choice of different lanthanide ions as sensitizer and activator is also very important. Typically, Yb^{3+} is always chosen as sensitizer because of its large absorption cross-section of around 980 nm. Er^{3+}, Tm^{3+}, and Ho^{3+} feature ladder-like arranged energy levels which favor multiphoton process, and thus are frequently used as activators.[25] Besides these three components, rational design of core–shell structure to minimize surface quenching effects and improve the luminescence efficiency of UCNPs is also very crucial.[25,70–72]

1.2.1 UCNPs Excited at 980 nm

The upconversion materials were first used in tissue imaging in 1999, when Zijlmans and coworkers reported the first upconversion bioimaging based on submicron-sized $Y_2O_2S:Yb^{3+}/Tm^{3+}$ particles (0.2–0.4 μm).[73] Upon excitation at 980 nm, they observed a low autofluorescence signal and no bleaching even after continuous exposure to high excitation energy levels. After that, the idea of upconversion bioimaging was realized by employing other oxysulfide or oxide nanomaterials (*e.g.*, $Y_2O_3:Yb^{3+}/Er^{3+}$ and $Gd_2O_3:Yb^{3+}/Er^{3+}$).[74,75] However, the size of the oxysulfide or oxide particles was at the submicron level, which limited applications. The necessary requirements for material selection in practical bioimaging are small size, bright luminescence, and biological safety. Recently, with the rapid development of synthesis techniques, fluoride-based UCNPs with smaller size but high-quality luminescence have been explored extensively and widely used in cell, tissue, and animal imaging. In contrast to oxysulfides or oxides, fluorides are considered better host materials for the doping of lanthanide ions to achieve intense UC emissions, owning to their low phonon energies and the resulting minimization of quenching of the excited state of the lanthanide ions. One of the first reports of *in vivo* imaging of UCNPs in small animals reported spot measurements of UCNPs injected subcutaneously in rats by Zhang *et al.* in 2008, which showed much deeper penetration under 980 nm excitation compared to commercial green-emitting QDs excited by UV.[76] Although the NIR excitation light for UC materials has strong penetration ability, the UV/VIS UC emissions are still easily absorbed by biological samples, which definitely limits their further applications in the observation of deep biological tissues. For small-animal *in vivo* imaging, highly sensitive NIR–NIR systems have attracted increasing attention, because both the excitation and emission light is located in the NIR region. For this purpose, Tm^{3+} ions are frequently chosen as dopants since they can exhibit strong NIR emission between 750 and 850 nm due to the transition from $^3H_4$ to $^3H_6$ under CW laser excitation at 980 nm. Nyk *et al.* reported the use of 20–30 nm $NaYF_4$ NPs doped with Tm^{3+} and Yb^{3+}, which has an emission around 800 nm for both *in vitro* and *in vivo* imaging (Figure 1.2).[77] High-contrast photoluminescence (PL) imaging was possible in cells and small animals due to the better tissue penetration properties achieved since both the excitation and emission are in the NIR region. After that, *in vivo* whole-body imaging of small animals has been successfully realized based on Tm^{3+}-doped $NaYF_4$,[78] $NaGdF_4$,[79] $NaLuF_4$,[80] and $NaYbF_4$ NPs.[81]

Besides 750–850 nm emission from Tm^{3+}, the red emission (625–690 nm, centered at 660 nm) from Er^{3+} or Ho^{3+} is also ideal for bioimaging. Therefore, much effort has also been devoted to enhancing the red emission of Er^{3+} or Ho^{3+}—in other words, to achieving an enhanced red/green (R/G) ratio in the Yb/Er codoped upconversion system. In 2011, Liu *et al.*[82] described an oil-based synthetic method for the preparation of $KMnF_3$ nanocrystals with lanthanide dopants homogeneously incorporated in the host lattice. With Yb^{3+}/Er^{3+} doping, blue and green emissions of Er^{3+} disappeared completely,

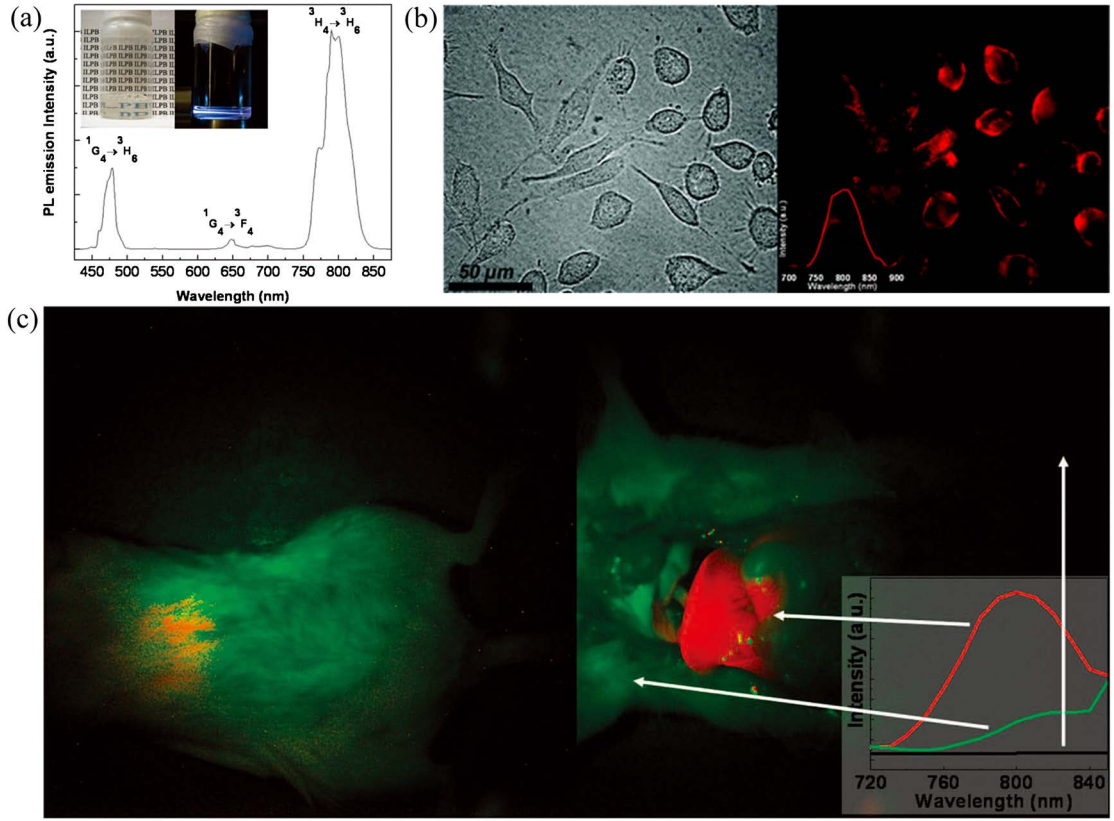

Figure 1.2 (a) PL spectra of $NaYF_4$:2% Tm^{3+},20% Yb^{3+} UCNPs in aqueous dispersion; excitation at 975 nm. Inset: sample of the UCNPs aqueous dispersion demonstrating colloidal stability, optical transparency, and efficient visible (blue) PL under excitation with 975 nm. (b) *In vitro* transmission (left) and PL (right) images of Panc 1 cells treated with UCNPs. Inset shows localized PL spectra taken from cells (red) and background (black). (c) Whole-body images of mouse injected intravenously with UCNPs; intact mouse (left), same mouse after dissection (right). The red color indicates emission from UCNPs, green and black show background as indicated by the arrows. The inset presents the PL spectra corresponding to the spectrally unmixed components of the multispectral image obtained with the Maestro system. (Reproduced with permission from M. Nyk, R. Kumar, T. Y. Ohulchanskyy, E. J. Bergey and P. N. Prasad, *Nano Lett.*, 2008, **8**, 3834–3838. Copyright (2008) American Chemical Society.)[77]

suggesting an extremely efficient exchange-energy transfer process between the Er^{3+} and Mn^{2+} ions, which can be largely attributed to the close proximity and effective mixing of wave functions of the Er^{3+} and Mn^{2+} ions in the crystal host lattices (Figure 1.3a). Besides Yb^{3+}/Er^{3+}, Yb^{3+}/Ho^{3+} and Yb^{3+}/Tm^{3+} doped $KMnF_3$ nanocrystals were synthesized, respectively. Importantly, these nanocrystals also displayed single-band emissions involving the $^5F_5 \rightarrow {}^5I_8$ (centered at 650 nm) transition in Ho^{3+} (Figure 1.3b) and the $^3H_4 \rightarrow {}^3H_6$ (centered at 800 nm) transition in Tm^{3+} (Figure 1.3c). As a result of efficient energy transfer between the dopant ion and host Mn^{2+} ion, remarkably pure single-band upconversion emissions were generated in the red and NIR spectral regions. The complete lack of short-wavelength emission of these lanthanide-doped nanocrystals in the visible spectral region provides a platform for promising applications in biolabeling studies, for which imaging at different sample depths is required. One year later, Zhao *et al.*[83] reported red-emission UCNPs based on $NaYF_4$ system, which is considered as one of the best host matrices for the upconversion process. In this work, Mn^{2+} served as a dopant to influence the growth dynamics of the crystalline phase and size of the resulting UCNPs, rather than host material. The Mn^{2+}-doped $NaYF_4$:Yb^{3+}/Er^{3+} (18/2 mol%) NPs were obtained by using a modified liquid–solid solution (LSS) solvothermal strategy: with the increased doping amount of Mn^{2+} ions, the phase transformation from hexagonal to cubic was obvious. Pure cubic $NaYF_4$ was obtained when the level of Mn^{2+} ions reached 5 mol% and no obvious extra diffraction peaks were detected even when the Mn^{2+} ion concentration increased to 30 mol%, indicating the formation of a Y–Mn solid solution. Interestingly, the R/G ratio gradually increased from 0.83 to 163.78 with increasing Mn^{2+} dopant content. The appearance of single-band red upconversion emission suggests that the exchange-energy transfer process between the Er^{3+} and Mn^{2+} ions is extremely efficient, which agrees with the conclusion from Liu *et al.* These red-emitting UCNPs can penetrate deeper than 10 mm when used for imaging *in vivo*, which is rarely reported in other papers (Figure 1.3d–f). Later in 2014, Hao *et al.*[84] extended these Mn^{2+}-doped UCNPs to other host materials, such as $NaLuF_4$ and $NaYbF_4$. They also observed large enhancements in overall UC luminescent spectra of Mn^{2+}-doped UCNPs (~59.1 times for the $NaLuF_4$ host, ~39.3 times for the $NaYbF_4$ host compared to the UCNPs without Mn^{2+} doping), mainly due to remarkably enhanced luminescence in the red band. Although great advances have been made in these three papers,[82–84] simultaneous control of the structure (nanocrystal size, shape, and phase) and enhancement in upconversion luminescence especially dominated by red emission in UCNPs with a fixed formula is still a great challenge. In 2015, Tian and his coworkers successfully synthesized a novel kind of small hexagonal-phase Mn^{2+}-doped $NaYbF_4$:Er^{3+} UCNPs with bright and red emission by a modified codeposition method.[85] This method was more controllable and convenient than the hydrothermal or solvothermal methods used previously[82–84] (Figure 1.3g–l). Moreover, Tian *et al.* found that the dopant Mn^{2+} ions have a negligible effect on the phase structure since all the diffraction peaks of the samples still correspond to

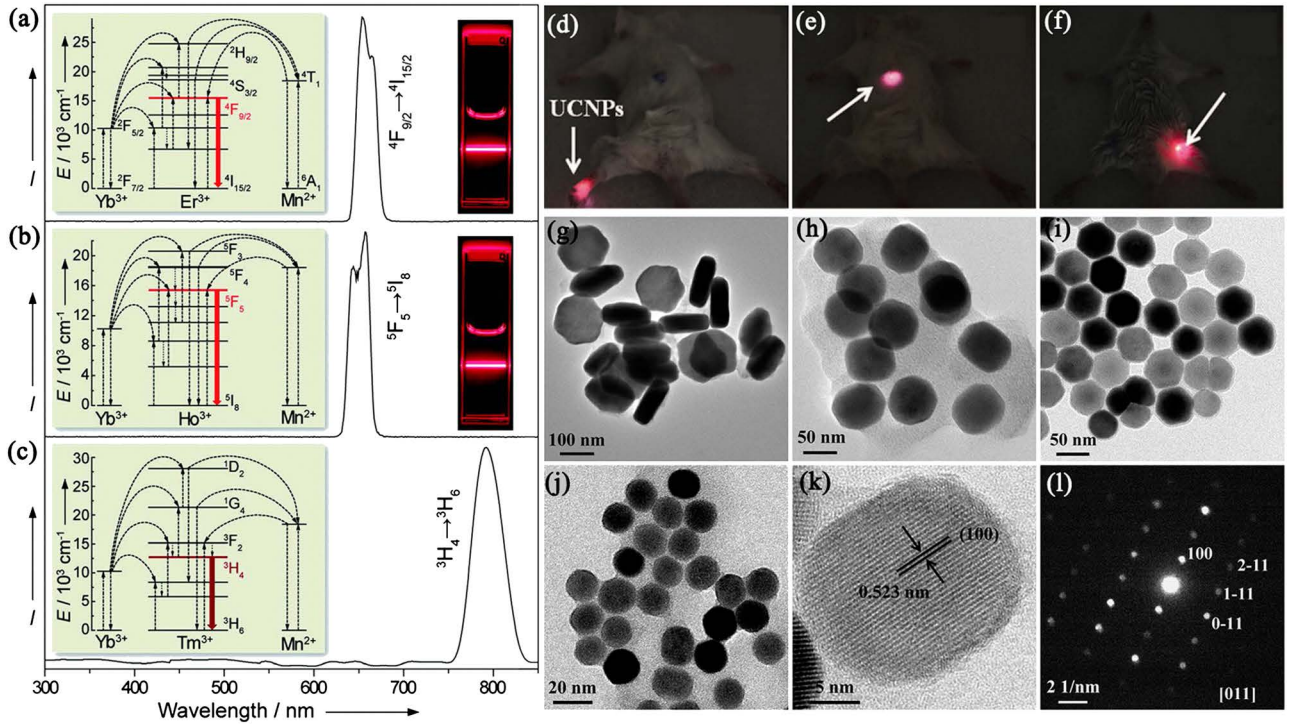

Figure 1.3 Room-temperature UC emission spectra of solutions containing: (a) $KMnF_3$:Yb/Er (18 : 2 mol%), (b) $KMnF_3$:Yb/Ho (18 : 2 mol%) and (c) $KMnF_3$:Yb/Tm (18 : 2 mol%) nanocrystals in cyclohexane (insets: proposed energy transfer mechanisms and corresponding luminescent photos of the colloidal solutions). (Reproduced from ref. 82 with permission from John Wiley and Sons. Copyright © 2011 Wiley-VCH Verlag GmbH & Co. KGaA, Weinheim.) (d–f) *In vivo* upconversion luminescence animal imaging using Mn^{2+}-doped $NaYF_4$:Yb^{3+}/Er^{3+} (18 : 2 mol%) NPs. (Reproduced with permission from ref. 83.) (g–l) TEM images of Mn^{2+}-doped $NaYbF_4$:Er^{3+} UCNPs obtained after heating for 1 h at 310 °C in the presence of 0, 10, 20, and 40 mol% Mn^{2+} dopant ions in (g), (h), (i), and (j), respectively. HRTEM and SEAD patterns of 40 mol% Mn^{2+} doping $NaYbF_4$:Er^{3+} UCNPs in (k) and (l). (Reproduced from ref. 85 with permission from the Royal Society of Chemistry.)

the pure hexagonal phase without admixture of cubic phase or other impurities. This finding was totally different from Zhao's and Hao's results, and it is well known that hexagonal-phase materials always exhibit higher upconversion efficiency relative to their cubic-phase counterparts. Therefore, Tian *et al.* concluded these hexagonal-phase Mn^{2+} doped $NaYbF_4$:Er^{3+} UCNPs may highly desirable in biomedicine, especially in bioimaging. Most recently, Rai *et al.*[86] reported significant enhancement in the red upconversion emission of Er^{3+} in $NaSc_{0.8}Er_{0.02}Yb_{0.18}F_4$ UCNPs through resonance energy transfer and plasmonic effect from Au NPs. Attachment of Au NPs on the surface of UCNPs gave two advantages: reduction in green band (through resonance energy transfer with efficiency 31.54%) and enhancement in red band (through the plasmonic effect). It gave a R/G ratio of nearly 20 : 1 (almost single-band red UC), which is quite promising for imaging applications.

1.2.2 Single-Band UCNPs

Single-band UCNPs have only one emission band under NIR excitation. Triply ionized lanthanide ions in UCNPs typically have emission line widths of 10–20 nm (FWHM) in the visible portion of the spectrum, which is approximately half the line width observed for QDs (25–40 nm) and much narrower than the line width observed for organic dyes (30–50 nm). This feature increases the number of distinguishable emission bands within a specific spectral bandwidth, enabling a large number of multiplexed detections. Although UCNPs have shown significant advantages over the traditional organic fluorophores or QD fluorescent biolabels, a problem remains: each lanthanide ion has a unique set of energy levels and generally exhibits a set of sharp emission peaks with distinguishable spectroscopic fingerprints. To minimize this spectral interference, in 2015 our group reported a general and simple method of achieving single-band upconversion emission with different colors by coating the upconversion nanocrystals with a screen layer containing an organic dye with a high molar absorption coefficient as a nanofilter to remove the unwanted emission bands.[87] As a result of the efficient reabsorption of the organic dye, remarkably pure single-band upconversion emissions can be generated in the blue, green, and red regions. The organic dyes were selected on the criteria of overlapping absorption spectra with only one of the dual emission bands of the nanocrystals, with a high molar absorption coefficient (in the range of 10^5 M^{-1} cm^{-1}). A pure silica spacer layer was used to prevent Förster resonance energy transfer (FRET) between the filtered upconversion emission band and the fluorescent dye-doped screen layer. To obtain green single-band emission, nickel(II) phthalocyanine-tetrasulfonic acid tetrasodium salt (NPTAT) organic dyes with a maximum absorption wavelength (λ_{max}) of 657 nm were added with tetraethyl silicate (TEOS) to form NPTAT-doped silica nanofilters on the β-$NaGdF_4$:20% Yb, 2% Er@$NaGdF_4$@SiO_2 NPs to filter the red emission band efficiently. With the β-$NaGdF_4$2:0% Yb, 2% Er@$NaGdF_4$@SiO_2@NPTAT-doped SiO_2 nanostructure, only the narrow green emission centered at 540 nm was observed, in

stark contrast to the dual upconversion emission bands of β-$NaGdF_4$:20% Yb, 2% Er@$NaGdF_4$. To obtain the blue and red emission single-band UCNPs, β-$NaGdF_4$2:0% Yb, 0.2% Tm@$NaGdF_4$, and α-$NaYbF_4$1:0% Er@$NaYF_4$ nanocrystals with strong blue to red and red-to-green upconversion emission ratios were first prepared. After coating the pure SiO_2 layers, nanofilters doped with NPTAT and rhodamine B isothiocyanate were used to filter the red and green emissions to obtain the final blue and red single-band UCNPs, respectively. This general approach permits not only the removal of minor emission peaks away from the main peaks using appropriate nanofilters, but also the alternative removal of the main peaks to leave the minor peaks for single-band upconversion emission. For example, green emission single-band UCNPs can be obtained by coating the α-$NaYbF_4$1:0% Er@$NaYF_4$ nanocrystals with NPTAT-doped nanofilters. Besides green (550 nm) emission single-band UCNPs, remarkably pure single-band upconversion emissions can also be generated in the blue (480 nm) and red (650 nm) regions.

Significantly, in this work, we have demonstrated the use of single-band UCNPs for the multiplexed detection of three tumor biomarkers in both cultured human breast cancer cells and paraffin-embedded clinical tissue sections. The simultaneous quantification of estrogen receptor (ER), progesterone receptor (PR), and HER2 receptor expression levels in the breast cancer cell specimens correlated closely with the results of the traditional western blot method. Furthermore, the application of conjugated single-band UCNPs and quantitative spectroscopy may be more accurate than immunoenzyme-based immunohistochemical (IHC) methods for the simultaneous quantification of proteins present at low levels in cancer cells and tissue specimens. Thus, single-band UCNP-based technology may be well suited to the molecular profiling of tumor biomarkers *in vitro* and represent a clinically translational application of upconversion nanomaterials for cancer prognosis. The ability to detect multiple target proteins in small samples of cancer tissues could enable more effective therapeutic decisions when used in combination with regular IHC methods. The next step is to conduct large-scale clinical studies to establish protocols and practices for single-band UCNP-based molecular pathology.

In the work discussed above, single-band UCNPs were used for multispectral *in vitro* biodetection, but we believe that single-band UCNPs may also hold great promise in multispectral bioimaging which requires no overlapping signals between different imaging agents (Figure 1.4).

1.2.3 UCNPs Excited at Another Wavelength Range

Traditionally, highly efficient UCNPs require a NIR laser at a wavelength of about 980 nm as the excitation source since the sensitizer ion (Yb^{3+}) has a high absorption cross-section in its absorption band. Unfortunately the 980 nm laser light is strongly absorbed by water and biological specimens. Thus, 980 nm excitation has associated problems such as limited penetration depth and tissue damage due to sample overheating. Therefore,

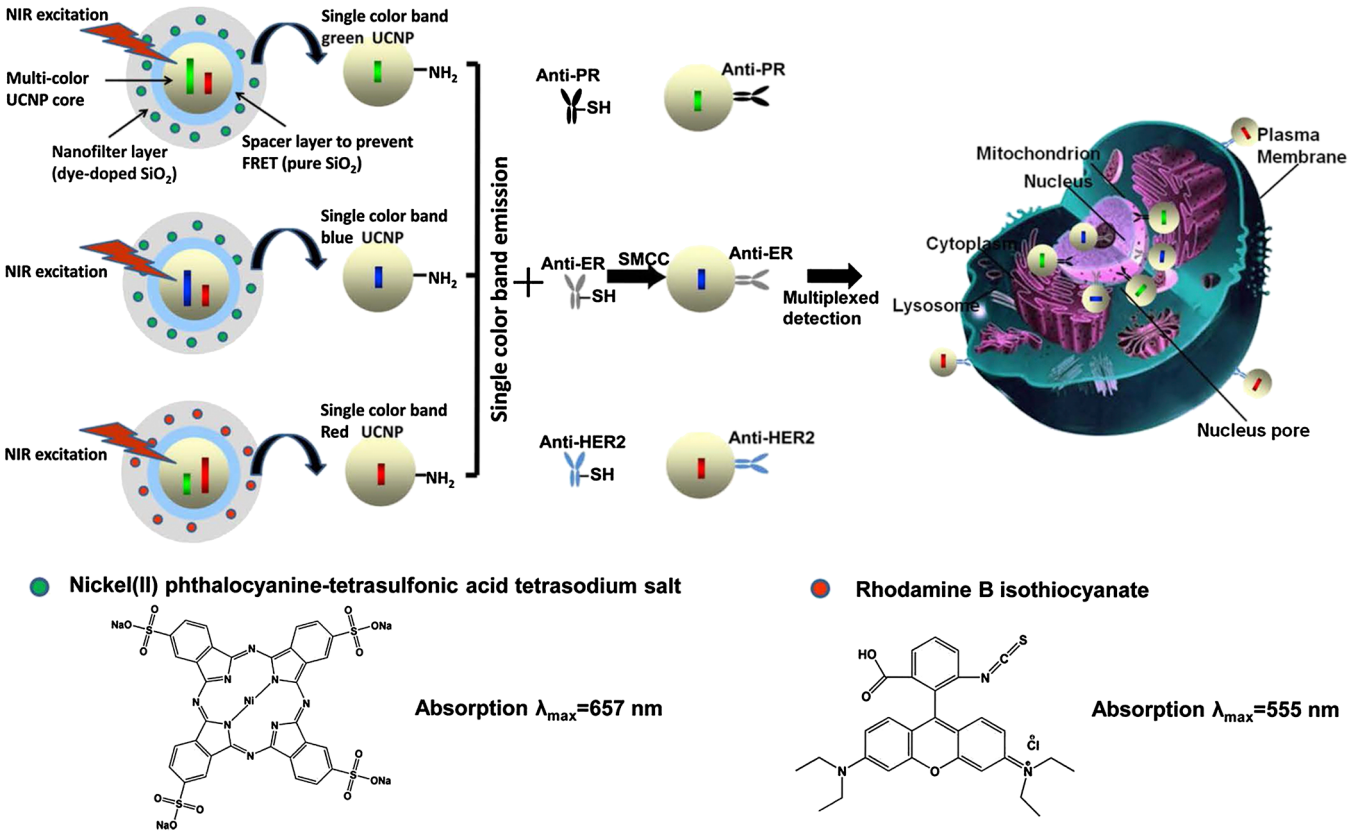

Figure 1.4 Schematic diagram of single-band UCNP fabrication for multiplexed detection. Surface amino modifications of the multilayer structure of green, blue, and red single-band UCNPs and conjugates with antibodies to the breast cancer biomarkers PR, ER, and HER2, respectively, for multiplexed *in situ* molecular mapping of breast cancer biomarkers. (Reproduced with permission from ref. 87.)

excitation band tuning of UCNPs into an appropriate range is also important for improving their performance. Zou *et al.* reported the concept of a UCNP where an organic NIR dye is used as an antenna to harvest the NIR photons within a broad band (740–850 nm) for the β-$NaYF_4$:Yb,Er NPs in which the upconversion occurs (Figure 1.5a). The overall upconversion by the dye-sensitized NPs is dramatically enhanced (by a factor of ~3300) as a result

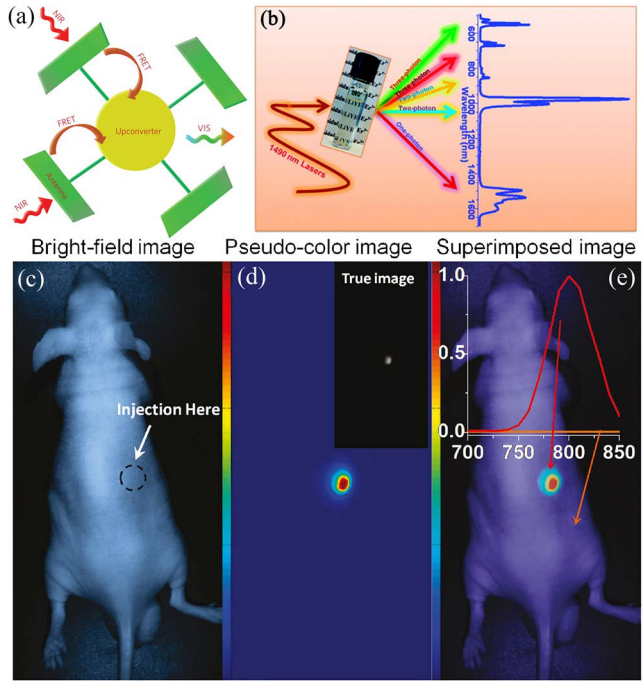

Figure 1.5 (a) Principal concept of the dye-sensitized nanoparticle. Antenna dyes (green) absorb NIR solar energy (red wavy arrows) and transfer it (brown arrows) to the nanoparticle core (in yellow), where upconversion occurs. Upconversion denotes a non-linear (on the incident radiation intensity) process in which the energies of two NIR quanta are summed to emit a quantum of higher energy in the green–yellow region (green–yellow wavy arrow). (Reproduced with permission from ref. 88.) (b) Intense visible and near infrared upconversion PL in colloidal $LiYF_4:Er^{3+}$ nanocrystals under excitation at 1490 nm. (Reproduced with permission from G. Y. Chen, T. Y. Ohulchanskyy, A. Kachynski, H. Agren and P. N. Prasad, *ACS Nano*, 2011, **5**, 4981–4986. Copyright (2011) American Chemical Society.[89]) (c–e) *In vivo* whole-body image of a NaYb-$F_4:Yb^{3+}/Tm^{3+}$ injected nude mouse: (c) bright field image; (d) pseudocolor image obtained from true image (the inset black/white image); (e) superimposed image (bright field image and pseudocolor image) with the unmixed spectra of *in vivo* image (the inset chart) of UC signal and background as indicated by the arrows. (Reproduced with permission from Q. Q. Zhan, J. Qian, H. J. Liang, G. Somesfalean, D. Wang, S. L. He, Z. G. Zhang and S. Andersson-Engels, *ACS Nano*, 2011, **5**, 3744–3757. Copyright (2011) American Chemical Society.[91])

of increased absorptivity and overall broadening of the absorption spectrum of the upconverter.[88] Prasad's group also reported the intense upconversion PL in colloidal $LiYF_4$:Er^{3+} nanocrystals under excitation at 1490 nm telecom wavelength (Figure 1.5b). The intensities of two- and three-photon anti-Stokes upconversion PL bands are higher than or comparable to that of the Stokes emission under excitation with low power density in the range 5–120 W cm^{-2}. The QY of the upconversion PL was measured to be as high as ~1.2 ± 0.1%, which is almost four times higher than the highest upconversion PL efficiency (0.3 ± 0.1%) reported to date for lanthanide-doped nanocrystals in 100 nm hexagonal $NaYF_4$:Yb^{3+},Er^{3+} using excitation at 980 nm.[89] Later in 2015, the same group reported a novel multilayer core–shell design to broadly upconvert infrared light at many discrete wavelengths into visible or NIR emissions. It utilized hexagonal-phase core/multishell $NaYF_4$:10% Er^{3+}@$NaYF_4$@$NaYF_4$:10% Ho^{3+}@$NaYF_4$@$NaYF_4$:1% Tm^{3+}@$NaYF_4$ NPs. These core–multishell NPs can emit UC PL emission from Ho^{3+} ($^5F_5 \rightarrow {}^5I_8$, 625–685 nm range), Tm^{3+} ($^3H_4 \rightarrow {}^3H_6$, 760–860 nm range), and Er^{3+} ($^4S_{3/2} \rightarrow {}^4I_{15/2}$, 510–570 nm range) when excited at ~1120–1190 nm (due to Ho^{3+}), ~1190–1260 nm (due to Tm^{3+}), and ~1450–1580 nm (due to Er^{3+}), respectively. The excitation light could collectively cover a broad spectral range of about 270 nm in the NIR range.[90] Zhan *et al.* also demonstrated a new and promising excitation approach for better NIR-to-NIR UC PL *in vitro* or *in vivo* imaging employing a cost-effective 915 nm laser. This novel laser excitation method led to much less heating of the biological specimen and greater imaging depth in the animals or tissues because water absorption was quite low (Figure 1.5c).[91]

1.2.4 Nd^{3+} Sensitized UCNPs

Recently, researchers have paid more attention to the 800 nm excitation UCNPs. Notably, Nd^{3+} has multiple NIR excitation bands at wavelengths shorter than 980 nm, such as 730, 808, and 865 nm, corresponding to transitions from $^4I_{9/2}$ to $^4F_{7/2}$, $^4F_{5/2}$, and $^4F_{3/2}$, respectively. At all of these wavelengths, water absorption is lower, and the typical absorption coefficient is 0.02 cm^{-1} at 808 nm, in contrast to 0.48 cm^{-1} at 980 nm.[92] Consequently, the laser-induced heating effect, especially for biological tissues, is expected to be greatly minimized. Meanwhile, Nd^{3+} has a large absorption cross-section in the NIR region (1.2×10^{-19} cm^2 at 808 nm) compared to that of Yb^{3+} (1.2×10^{-20} cm^2 at 980 nm), which also benefits the efficiency of the Nd^{3+}-sensitized upconversion process.

Han *et al.* found when Nd^{3+}, Yb^{3+}, Er^{3+}/Tm^{3+} were codoped in $NaYF_4$, upconversion distinguishable by the naked eye can be observed upon the 800 nm excitation (Nd^{3+} has a broad excitation wavelength in the range of 790–810 nm). In these novel UCNPs, Nd^{3+} serves as an 800 nm photon sensitizer and Yb^{3+} as a bridging ion, with the energy transfer procedure performing as $Nd^{3+} \rightarrow Yb^{3+} \rightarrow Er^{3+}$/$Tm^{3+}$. However, the doping limit of the Nd^{3+} is only 1% because of concentration quenching.[93] Apparently, novel structure needs to be designed to increase the doping concentration of Nd^{3+}. In 2013, Liu

et al. reported a new type of core–shell UCNPs (Figure 1.6a). Through spatially confined doping of Nd^{3+}, which can be effectively excited at 795 nm, they claimed that the active $NaYF_4$:Nd^{3+} shell layer can effectively prevent surface quenching of Yb^{3+} emission and can simultaneously promote the transfer of excitation energy to Yb^{3+} ions, which significantly enhances the

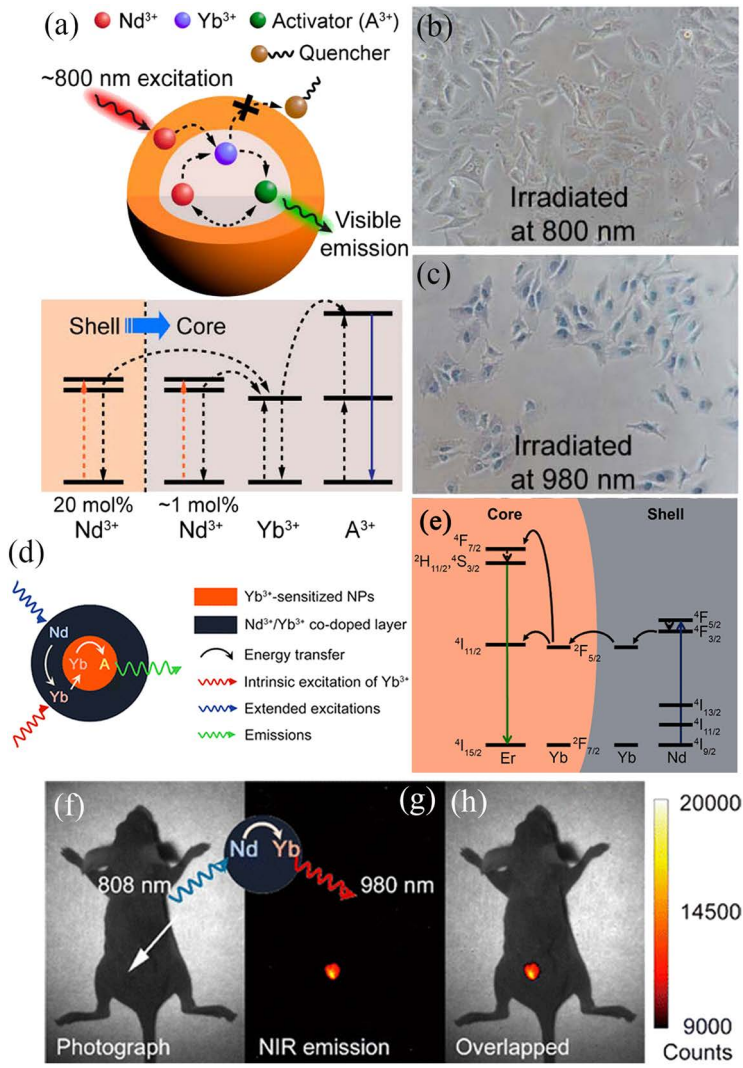

Figure 1.6 (a) Schematic design (top) and simplified energy level diagram (bottom) of a core–shell nanoparticle for photon upconversion under 800 nm excitation. Nd^{3+} ions doped in the core and shell layers serve as sensitizers to absorb the excitation energy and subsequently transfer it to Yb^{3+} ions. After energy migration from the Yb^{3+} ions to activator ions, activator emission is achieved *via* the Nd^{3+}-sensitization process. (b and c) Optical microscopy images of trypan blue-treated HeLa cells

upconversion; also, 800 nm is better than 980 nm for heat generation, as confirmed by cell irradiation experiment (Figure 1.6b and c).[94] Almost at the same time, Yan and his co-workers reported a similar core–shell structure (Figure 1.6d) with a similar design idea by doping Nd^{3+} in the shell to ensure successive $Nd^{3+} \rightarrow Yb^{3+} \rightarrow$ activator energy transfer. *In vivo* imaging of a nude mouse subcutaneously injected with UCNPs showed that comparable photon numbers can be measured when irradiated with 980 nm laser and 808 nm laser, respectively (Figure 1.6e). In addition to the upconversion process, these authors also performed downconversion PL of lanthanide-doped NPs. *In vivo* NIR imaging of a nude mouse injected with UCNPs showed high signal-to-noise ratio under 808 nm laser excitation (Figure 1.6f–h).[95]

These results indicate that excitation at 800 nm is indeed a good future direction for development of UCNPs in biomedical imaging. However, more theoretical research has shown that the efficiency limitation of Nd^{3+}-sensitized UCNPs is the "energy back-transfer" phenomenon, which can efficiently transfer energy from activators back to ^4I_J manifolds of Nd^{3+}, such as from Er^{3+} to Nd^{3+}. As a result, the doping concentration of Nd^{3+} in UCNPs must be constrained to a very low level (<1%) to minimize the quenching of the excitation energy. Therefore, directly doping Nd into UCNPs always results in much lower upconversion luminescence under 800 nm NIR laser irradiation than that of the conventional 980 nm-excited UCNPs in the same conditions.

In 2014, a breakthrough was made by Zhao's group. They first developed a well-defined $NaYF_4$:Yb,X@$NaYF_4$:Yb@$NaNdF_4$:Yb (X = Er^{3+}, Tm^{3+}, Ho^{3+}) core–shell–shell structure (Figure 1.7a and b) to separate the activator (Er^{3+}, Tm^{3+}, Ho^{3+}) and sensitizer (Nd^{3+}) into different layers, which enables efficient harvesting of NIR light, suppresses the cross-relaxation between the sensitizer and activator, and finally results in the generation of efficient upconversion emissions under 800 nm CW laser excitation (Figure 1.7c).[96] They found that the emission intensity of $NaYF_4$:Yb,Er@$NaYF_4$:Yb@$NaNdF_4$:Yb core–shell–shell (ErCSS) NPs (~16 nm) with optimized shell thickness shows enhancement factors of ~2000 (compared with the conventional $NaYF_4$:Yb,Er@$NaYF_4$

recorded after irradiation for 5 min at 800 and 980 nm, respectively (6 W cm^{-2}). (Reproduced with permission from X. J. Xie, N. Y. Gao, R. R. Deng, Q. Sun, Q. H. Xu and X. G. Liu, *J. Am. Chem. Soc.*, 2013, **135**, 12608–12611. Copyright (2013) American Chemical Society.[94]) (d) Integration scheme of $Nd^{3+} \rightarrow Yb^{3+}$ energy transfer process by introducing Nd^{3+}/Yb^{3+} codoped shell. The resulting $Nd^{3+} \rightarrow Yb^{3+} \rightarrow$ activator energy transfer could extend the effective excitation bands for conventional Yb^{3+}-sensitized UCNPs. (e) Energy transfer pathway from Nd^{3+} to Yb^{3+}-activated Er^{3+} upconversion emission in core–shell structured NPs under 808 nm excitation. (f–h) *In vivo* NIR imaging of a nude mouse injected with Er@Nd NPs dispersed in water. (f) White-light photograph, (g) NIR image obtained with 808 nm excitation, and (h) overlapped image. Injection site is denoted by the white arrow. (Reproduced with permission from Y. F. Wang, G. Y. Liu, L. D. Sun, J. W. Xiao, J. C. Zhou and C. H. Yan, *ACS Nano*, 2013, **7**, 7200–7206. Copyright (2013) American Chemical Society.[95])

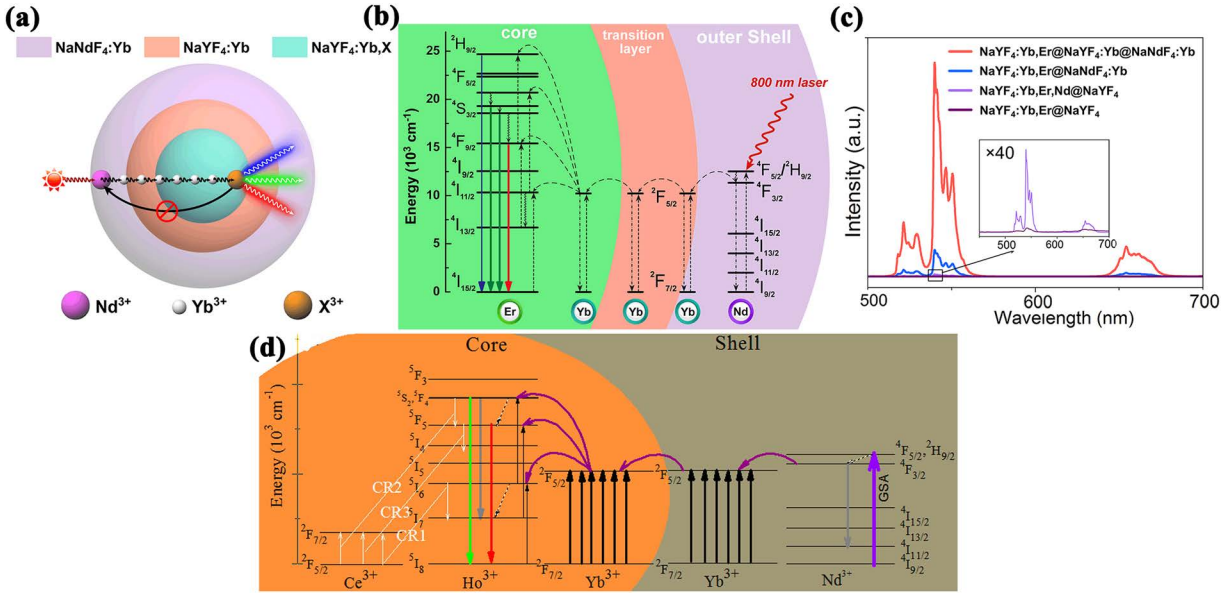

Figure 1.7 (a) Schematic illustration of the proposed energy-transfer mechanisms in the quenching-shield sandwich-structured UCNPs upon 800 nm excitation. (b) Proposed energy-transfer mechanisms in the quenching-shield sandwich NPs upon 800 nm diode-laser excitation. (c) Upconversion emission spectra of the synthesized quenching-shield sandwich NPs (red line), the Nd-coating core–shell NPs (blue line), the Nd/Yb/Er triply doped NPs (violet line), and the conventional Yb^{3+}-sensitized UCNPs (dark violet line) under 800 nm excitation (0.5 W cm^{-2}). (Reproduced from ref. 96 with permission from John Wiley and Sons. Copyright © 2013 Wiley-VCH Verlag GmbH & Co. KGaA, Weinheim.) (d) Energy level diagrams of Ce^{3+}, Ho^{3+}, Yb^{3+}, and Nd^{3+} as well as the proposed mechanisms for the achievement of pure red UC luminescence under 980 or 808 nm laser excitation in Yb/Ho/Ce:$NaGdF_4$@Yb/Nd:$NaYF_4$ core–shell NPs. (Reproduced with permission from D. Chen, L. Liu, P. Huang, M. Ding, J. Zhong and Z. Ji, *J. Phys. Chem. Lett.*, 2015, **6**, 2833–2840. Copyright (2015) American Chemical Society.[97])

core–shell (ErCS) NPs), ~100 (compared with the Nd/Yb/Er tri-doped UCNPs) and ~8 (compared with the Nd-coated core–shell UCNPs) under 800 nm irradiation. Notably, the upconversion emission of the 800 nm-excited ErCSS NPs (~16 nm) is ~7 times higher than that of the conventional 980 nm-excited ErCS NPs (~20 nm, hexagonal phase) at a low excitation power (0.1 W). Moreover, other lanthanide ions conventionally used for generating upconversion emissions, including Tm^{3+} and Ho^{3+}, can also serve as the activator in an Nd^{3+}-sensitized core–shell–shell system (Tm: TmCSS; Ho: HoCSS), because the efficient energy transfer from Yb^{3+} to these lanthanide ions can still be facilitated. Similar enhanced upconversion emission could be observed in Tm (~4.6 times) and Ho (~2 times) doped core–shell–shell nanocrystals. An explanation of the high efficiency is that the Nd^{3+} and the activators (Er^{3+}, Tm^{3+}, Ho^{3+}) were separated by a core–shell structure, in which the Nd^{3+} was confined in the shell and the activators were embedded in the core. Therefore, the non-radiative processes resulting from Er–Nd interactions are largely impeded. These characteristics lead the authors to believe that these 800 nm-excited core–shell–shell NPs with improved optical performance will outperform conventional 980 nm-excited UCNPs and play an important role in the development of fluorescent probes for future bioimaging applications.

Recent advances in Nd^{3+}-sensitized UCNPs are 800 nm-excited UV/blue and red light, which are considered good light sources for stimulation–response systems (such as controlled drug delivery or photodynamic therapy) and bioimaging, respectively. In 2013, Wang *et al.* reported 808 nm-excited UV/blue emission from a novel $NaYbF_4$:50% Nd@Na(Yb,Gd)F_4:Tm^{3+}@$NaGdF_4$ core–shell–shell nanoparticle.[98] They claimed that the appearance of upconversion emission peaks in the UV spectral region is largely owing to the core–shell structure, which suppresses deleterious cross-relaxations in the NPs. When the Tm^{3+} was homogenously doped with Yb^{3+} and Nd^{3+} ions in the core layer, UV upconversion emission peaks essentially disappeared. Strikingly, for the first time they realized UV emission of Tm^{3+} at around 300 nm in NPs by 808 nm diode laser excitation through careful control of the doping concentration of Tm^{3+}. In addition, the establishment of a population at a high-lying energy state of Tm^{3+} also further enables an energy cascade in the Gd sublattice followed by energy trapping and optical emission from common lanthanide ions including Tb^{3+}, Eu^{3+}, and Dy^{3+}. Later in 2015, they applied their core–shell–shell nanostructure in 800 nm-excited red UCNPs.[99] They have assessed a series of $NaYbF_4$:Nd@$NaGdF_4$:Yb/Er@$NaGdF_4$ NPs with varying Yb^{3+} concentrations in the inner shell layer. The red emission of Er^{3+} gradually dominated the spectra with increasing Yb^{3+} concentration from 18 to 78 mol%, which corresponds to intensity ratios of red-to-green emission from 0.5 to 0.7, 0.85, and 1.9. The steady increase in the red/green ratio was mainly induced by the $^4S_{3/2} + {}^2F_{7/2} \rightarrow {}^4I_{13/2} + {}^2F_{5/2}$ and $^4I_{13/2} + {}^2F_{5/2} \rightarrow {}^4F_{9/2} + {}^2F_{7/2}$ cross-relaxations at elevated Yb^{3+} concentrations. Further increasing Yb^{3+} concentration did not lead to noticeable improvement in red emission of Er^{3+}, probably due to the poor shell quality as a result of the fast shell deposition process in the absence of Gd^{3+} cofactors. They also examined relevant

NPs comprising high concentrations of Er^{3+} in the inner shell layer, which are known to induce $^4S_{3/2} + {}^4I_{9/2} \rightarrow {}^4F_{9/2} + {}^4F_{9/2}$ cross-relaxation between Er^{3+} ions for promoting the red emission of Er^{3+}. PL investigation showed that the emission spectra of Er^{3+} can only be marginally tuned by varying the Er^{3+} concentration, accompanied by a decrease in the overall emission intensity at high Er^{3+} content. Taken together, the optimal Yb/Er concentration was determined to be 78/2 mol%. In their *in vitro* experiment, they found the optical emission can be clearly observed when a 5 mm sample of pork muscle tissue is placed between the cells and the irradiating laser. The upconversion emission signals were still detectable after the thickness of the muscle tissue was increased to 10 mm. As a control experiment, classical $NaYF_4$:Yb/Er (18/2 mol%)@$NaYF_4$ core–shell NPs can hardly be detected when the laser beam is blocked by a muscle tissue as thin as 5 mm. Almost at the same time, Chen *et al.* presented another strategy to achieve 808 nm-excited single-band red upconversion luminescence of Ho^{3+} *via* Ce^{3+} to change the red/green ratio in the $NaGdF_4$:Yb/Ho/Ce@Yb/Nd:$NaYF_4$ active-core@active-shell nanoarchitecture (Figure 1.7d).[97] The doping of Ce^{3+} plays a key role in the realization of Ho^{3+} single-band red luminescence *via* the efficient cross-relaxation processes between Ce^{3+} and Ho^{3+}: that is, Ho^{3+5}:$S_2/{}^5F_4 + Ce^{3+2}$:$F_{5/2} \rightarrow Ho^{3+5}$:$F_5 + Ce^{3+2}$:$F_{7/2}$ and Ho^{3+5}:$I_6 + Ce^{3+2}$:$F_{5/2} \rightarrow Ho^{3+5}$:$I_7 + Ce^{3+2}$:$F_{7/2}$. This nanoarchitecture enables the spatial separation between Ho^{3+} and Nd^{3+} and subsequently the high-content Nd^{3+} doping to efficiently improve upconversion luminescence, which might finally provide highly attractive luminescent biomarkers for bioimaging without the problematic overheating effect.

1.3 Lanthanide Downconversion Nanoparticles (DCNPs)

Lanthanide-based NIR downconversion nanoparticles (DCNPs) emerged a little later than UCNPs. The synthesis and surface modification procedures successfully used for UCNPs can also be well utilized on DCNPs. Ions of almost all the 15 lanthanide possess the downconversion property, and their emission wavelength can be located in the UV, visible, NIR I, NIR II and even mid-IR range.[100–102] Typically, 865–900 nm, 1060 nm, and 1300 nm from Nd^{3+} ($^4F_{3/2} \rightarrow {}^4I_{9/2}$, $^4F_{3/2} \rightarrow {}^4I_{13/2}$, and $^4F_{3/2} \rightarrow {}^4I_{15/2}$, respectively), 900–1000 nm from Yb^{3+} ($^2F_{5/2} \rightarrow {}^2F_{7/2}$), 1185 nm from Ho^{3+} ($^5I_6 \rightarrow {}^5I_8$), 1310 nm from Pr^{3+} ($^1G_4 \rightarrow {}^3H_5$), 1475 nm from Tm^{3+} ($^3H_4 \rightarrow {}^3F_4$), and 1525 nm from Er^{3+} ($^4I_{13/2} \rightarrow {}^4I_{15/2}$) are common NIR emission wavelengths in the spectral database of the lanthanide ions. However, the luminescence efficiency of these wavelengths varies greatly, and developing efficient DCNPs with proper emission wavelengths is an important issue in this field.

The first attempts to utilize DCNPs as biomedical imaging agents (NIR I or NIR II) have been made in the last decade. As early as 2002, Veggel *et al.* reported Nd^{3+}-doped LaF_3 NPs with both NIR I and NIR II emission under 514 nm laser excitation, as well as Er^{3+}- or Ho^{3+}-doped NPs. Because the

interesting luminescence emission is in the telecommunication window (*i.e.*, Er^{3+} at 1530 nm, Nd^{3+} at 1330 nm, and Ho^{3+} at 966 nm and 1450 nm), they had considered them as promising materials for polymer-based optical components.[103] In 2006, inspired by Veggel's work, Wang *et al.* developed a simple method to synthesize LaF_3:Nd^{3+} in aqueous solution at low temperature, and have pointed out that this kind of DCNP would have potential application in biomedical imaging. The emission of Nd^{3+}-doped LaF_3 nanocrystals is located in NIR II under 802 nm laser excitation.[104] Later in 2008, NdF_3 NPs were synthesized in aqueous solution by a similar method as used to synthesize traditional Nd^{3+}-doped LaF_3 NPs. NdF_3 NPs showed no doping concentration quenching effect; moreover, the vibrational quenching caused by the O–H groups on the surfaces of the NdF_3 NPs can be suppressed after coating with silica shells. For deep-tissue imaging, mice were injected intramuscularly and intraperitoneally with 100 μL of NdF_3/SiO_2 NPs (1.0 μg mL^{-1}) into the thigh and abdominal cavity respectively. NIR signals (1050 nm) from the deep tissues of the thigh and abdominal cavity can both be clearly distinguished from the tissue autofluorescence under 730 nm excitation.[105] Later in 2013, Nd^{3+}-doped DCNPs based on a GdF_3 host matrix were realized by Mimun *et al.*[106] The GdF_3:Nd^{3+} NPs were small, with an average size of 5 nm, and formed stable colloids that lasted for several weeks without settling, enabling their use for several biomedical and photonic applications. Their excellent NIR properties, such as a nearly 11% QY the 1064 nm emission, make them ideal contrast agents and biomarkers for *in vitro* and *in vivo* NIR optical bioimaging. The nanophosphors, which were coated with poly(maleic anhydride-*alt*-1-octadicene) (PMAO), were implemented in cellular imaging, showing no significant cellular toxicity for concentrations up to 200 mg mL^{-1}. A proof-of-concept experiment for imaging through tissue was conducted by placing the GdF_3:Nd^{3+} NPs under varying thicknesses of pig skin, ranging from 0.67 to 5 mm. Emission spectra were collected through each thickness, and the 1064 nm emission was easily discernible even at the greatest tissue thickness of 5 mm. Furthermore, the incorporation of Gd into the nanocrystalline structure endowed these NPs with exceptional magnetic properties, making them ideal for use as magnetic resonance imaging (MRI) contrast agents. Almost at the same time, the same group reported their investigation of the downconversion absolute quantum yields measurement on the powder, PMAO-coated powder, and colloidal solution states of GdF_3:Nd^{3+} NPs.[107] The maximum total absolute downconversion QY of 10.2 ± 1.5% was measured for the GdF_3:Nd^{3+} nanophosphor powder at an excitation power density of 12.74 ± 2.0 W cm^{-2} at 800 nm excitation. Similarly, downconversion QYs of 5.02 ± 0.75% and 2.2 ± 0.33% were measured at an excitation power density of 5.3 ± 0.8 and 1.4 ± 0.2 W cm^{-2}, respectively. With the known QY 10% for IR-140 dye in the spectral range of 862–1013 nm at an excitation power of 150 mW under 800 nm excitation, a comparison method was also implemented to check the accuracy of the measurement. Comparison measurement for GdF_3:1% Nd^{3+} powder shows that the downconversion QY in GdF_3:1% Nd^{3+} is 5.8 ± 0.87% at 150 mW (4.77 W cm^{-2}) excitation under

800 nm, which is very close to the measured QY at 5.3 W cm^{-2} using integrating spheres for GdF_3:1% Nd^{3+} powder. Scaling of the downconversion emission spectra revealed that the 1064 nm emission from Nd^{3+} represents around 90% of the overall downconversion emission intensity. In addition, compared with the upconversion QY of 0.005 ± 0.0005% (at 150 W cm^{-2}) reported by van Veggel *et al.* for β-$NaYF_4$:20% Yb^{3+}/2% Er^{3+} of 8–10 nm sized particles, the downconversion QY for GdF_3:1% Nd^{3+} nanophosphor powder is 2000 times higher even at an excitation power density of 12.74 ± 2.0 W cm^{-2} at 800 nm excitation.[108] This shows that these particles have a higher QY within the biological window which yield more photon counts (information density) for bioimaging applications compared to UCNPs. Furthermore, the comparison method was implemented to measure the downconversion QY for colloidal GdF_3:1% Nd^{3+} with respect to the reported QY for the dye IR-140 to mimic the experimental conditions. Using the QY of 10% reported for the IR-140 at 150 mW (4.77 W cm^{-2}) excitation under 800 nm, the downconversion QY for GdF_3:1% Nd^{3+} at a concentration of 0.05 mg mL^{-1} was measured to be 1 ± 0.05%. Similarly, the QY of 1.5 ± 0.075% was measured for GdF_3:1% Nd^{3+} at 255 mW (8.28 W cm^{-2}). This verifies that the QY for colloidal GdF_3:1% Nd^{3+} is dependent on concentration and excitation power density, indicating that DCNPs yield more photon counts (information density) for bioimaging applications than UCNPs. The authors also have measured the NIR emission spectra obtained with and without the additional PMAO coating for the GdF_3:1% Nd^{3+} at an excitation power density of 12.74 ± 2.0 W cm^{-2}. Coating the NPs with PMAO does not significantly change the measured downconversion QY, which is important since the polymer coating is essential for making the particles biocompatible.

Although considerable research has been done on LaF_3:Nd^{3+}, GdF_3:Nd^{3+}, and NdF_3, morphology control of the NPs is still a big problem for this type of materials. Thanks to the well-developed synthesis methods for UCNPs, uniform and monodispersed $NaReF_4$:Nd^{3+} NPs (where Re = rare earth elements) have been obtained, and have attracted increasing attention in recent years.[109–111] In 2012, Prasad *et al.* reported highly efficient $NaGdF_4$:Nd^{3+}@$NaGdF_4$ for NIR–NIR biomedical imaging.[112] Unlike LaF_3:Nd^{3+}, these novel DCNPs benefit from controllable morphology and even ~3 nm uniform $NaGdF_4$ shells have been successfully synthesized (Figure 1.8a). These DCNPs exhibited spectrally sharp, photostable, and large Stokes-shifted NIR PL at 900, 1050, and 1300 nm when excited at 740 nm (Figure 1.8b). The absolute QY of this NIR-to-NIR downconversion PL was evaluated to be as high as 40% for core–shell $NaGdF_4$:Nd^{3+}@$NaGdF_4$ NPs dispersed in hexane and 20% for ligand-free $NaGdF_4$:Nd^{3+}@$NaGdF_4$ NPs dispersed in water. The high luminescent efficiency in NPs was realized by effective suppression of non-radiative losses originating from surface passivation and cross-relaxation between Nd^{3+} dopants, as revealed by the PL steady-state and time-resolved studies. A facile high-contrast NIR-to-NIR imaging of HeLa cells and a nude mouse were demonstrated by the authors, utilizing excitation from an incoherent light source through observation of NIR PL at 900 nm (Figure 1.8c–e).

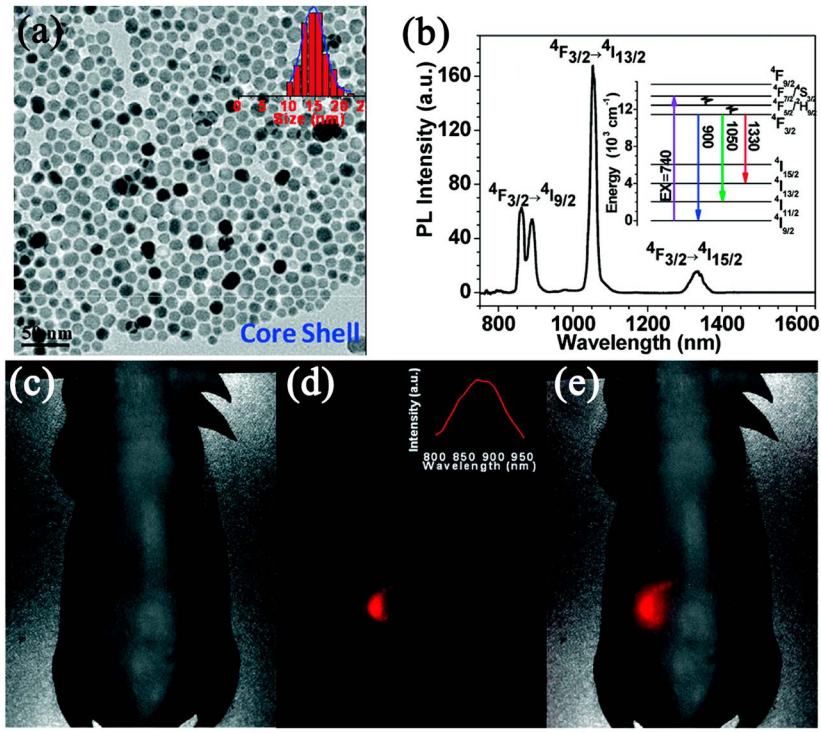

Figure 1.8 (a) TEM images of $NaGdF_4$:Nd^{3+}@$NaGdF_4$ core–shell nanocrystals. (b) PL spectrum of colloidal $NaGdF_4$:Nd^{3+} nanocrystals under laser excitation at 740 nm. The inset shows the mechanism of generation of the observed PL emissions. (c–e) *In vivo* whole-body image of a nude mouse subcutaneously injected with ligand-free $NaGdF_4$:Nd^{3+}@$NaGdF_4$ core–shell nanocrystals: (c) bright field image, (d) PL image, and (e) superimposed image (bright field image and spectrally unmixed PL image). Inset in (d) is the spectra of the NIR PL signals with a background taken from the injection site and noninjected area. (Reproduced with permission from G. Y. Chen, *et al.*, *ACS Nano*, 2012, **6**, 2969–2977. Copyright (2012) American Chemical Society.[112])

Recently, some attempts have been made to explore the downconversion optical property of the traditional UCNPs. Nagasaki *et al.* had reported the application of Y_2O_3:Yb^{3+},Er^{3+} as a UCNP biomedical imaging nanoprobe in 2008.[113] In 2011, they used the same kind of NPs for the downconversion bioimaging research. A strong NIR signal (1550 nm) can be observed 24 h after intravenous injection of DCNPs upon the irradiation of 980 nm laser.[114] Although this work is at an early stage, it also indicates that other lanthanide ions, such as Er^{3+}, may hold promise for NIR bioimaging. Er^{3+} possesses a stable energy level in the NIR range ($^4I_{13/2}$), which can emit NIR light in the wavelength range of 1450–1650 nm. In 2014, exciting work on the downconversion phenomenon of UCNPs was published by Moghe and his colleagues. They first developed a library of rare earth nanomaterials with tunable,

discrete SWIR (short-wavelength infrared, 1000–2300 nm, including NIR II) emissions and proceeded to evaluate their optical performance for several clinical imaging applications including real-time, multispectral *in vivo* SWIR imaging.[115] The rare earth nanomaterials they used were $NaYF_4$:Yb^{3+}, Ln^{3+} (Ln = Er, Ho, Tm, or Pr)@$NaYF_4$ core–shell NPs. By doping the $NaYF_4$ core with Yb and one of several other rare earth elements, such as Er, Ho, Tm, or Pr, the emission properties of rare earth nanomaterials can be tailored in both the SWIR and visible ranges. The fluorescence of rare earth nanomaterials occurs following the resonant transfer of excitation energy from a sensitizer (Yb) to an activator dopant such as Er, Ho, Tm, or Pr. The relaxation from an excited state results in the generation of SWIR emissions that are unique to the specific rare earth activator. Hexagonal-phase $NaYF_4$:Yb^{3+},Er^{3+} NPs were among the brightest SWIR-emitting rare-earth-doped phosphors (with an optical efficiency >1.1%), and therefore were chosen to illustrate not only the benefits of SWIR compared to conventional optical imaging methods but also the biomedical potential for SWIR-based imaging approaches. Compared to other SWIR emitters, the rare earth nanomaterials presented in this work are considerably more effective at generating SWIR emissions than single-walled carbon nanotubes (SWNTs) and IR-26, an organic SWIR dye. Only highly toxic lead-based QDs matched the SWIR emission power output of the rare earth nanomaterials. This group further investigated the attenuation properties of actual biological tissues in the SWIR by measuring the absorbance spectra of excised tissue obtained from a mouse exhibiting pigmented tumor lesions. The majority of tissue samples exhibit markedly low attenuation at 1000–1350 nm as well as at 1500–1650 nm, effectively extending the wavelength region of lowered attenuation within the second 'tissue-transparent window' of SWIR. Furthermore, strong absorbers in the tissue, such as melanin in tumor samples and hemoglobin in blood samples, exhibited strong attenuation in the visible range whereas attenuation in the SWIR was weak. Importantly, <0.4% of NIR I light penetrated through 0.5 cm of pigmented tumor tissue compared to ~80% transmittance achieved by SWIR, suggesting that NIR I has limited use for detecting optical probes in melanin-containing tissues. Furthermore, they determined the actual tissue penetration depth of SWIR compared to the current standard imaging wavelength region by measuring the intensity of SWIR and NIR I light through tissue phantoms composed of both scattering and absorbing agents. The intensity of the NIR I signal rapidly diminishes over increasing phantom depth, with complete signal loss occurring by 5 mm. In contrast, the high SWIR emission from the rare earth nanomaterial pellet saturates the camera's detector for phantom tissues at 5 mm or less. Notably, SWIR signal was detectable through 1 cm of phantom tissue, whereas no signal above background was seen using NIR I. In the *in vivo* SWIR imaging experiment, rare earth nanomaterials also showed good performance. Using a series of image-processing algorithms, SWIR signal intensities as a function of concentration of rare earth nanomaterials were found to exhibit a linear relationship in both tissue phantoms and subcutaneously injected mice, with a detection threshold at ~3 nM rare

earth nanomaterials at an excitation power density of 0.14 W cm^{-2} and camera exposure time of ~50 ms per frame. In comparison to QDs and SWNTs with reported detection limits of ~5 nM and 6 nM respectively, rare earth nanomaterials can be detected at a lower concentration under comparable excitation. After injection, SWIR emissions were first identified in the tail vein (5 s) before clearing the vasculature to enter the heart and lungs (10 s). The beating of the heart in the chest of the mouse was visualized by pulsing SWIR emissions captured in real time (Figure 1.9). Over the course of 60 s, the SWIR signal became progressively more intense in organs such as the liver and spleen, which are part of the reticuloendothelial system that mediates nanoparticles. In contrast, the accompanying visible signal from UCNPs was notably absent, probably due to absorption and scattering losses caused by blood and tissue components.

Although great advances have been made by Moghe and his colleagues, 980 nm-excited lanthanide-based NIR nanomaterials, both UCNPs and DCNPs, suffer from the same problem: the water in biological structures

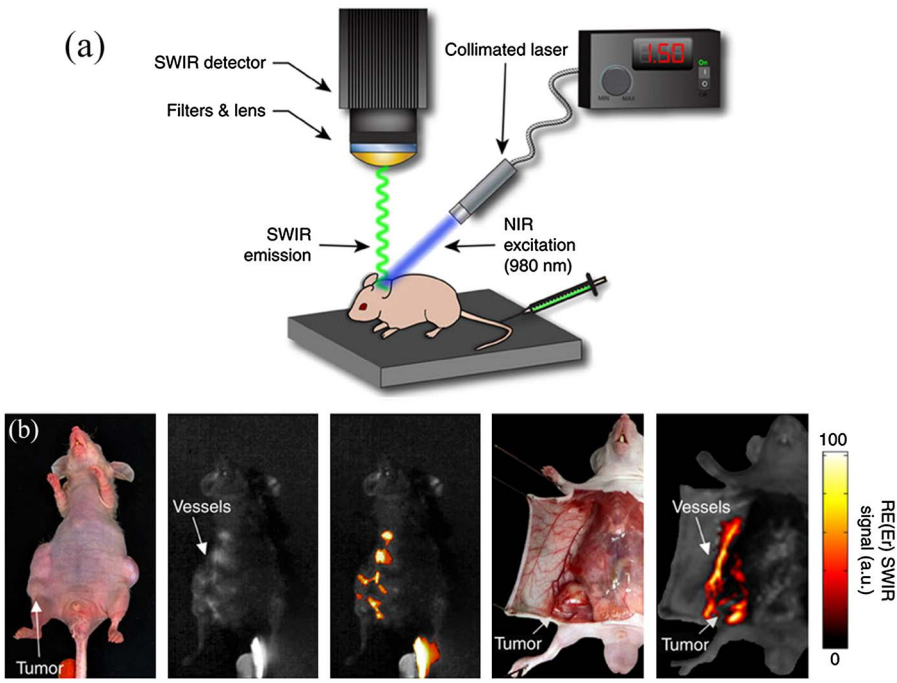

Figure 1.9 (a) Schematic of the portable SWIR imaging prototype, consisting of a room temperature-cooled InGaAs camera operating at a typical exposure time of 50 ms, adjustable filter mounts, a collimated laser with an output power density of 0.14 W cm^{-2}, and a neoprene rubber imaging surface. (b) Nude mice bearing melanoma xenografts were intravenously injected with rare earth nanomaterials and imaged near surrounding tumor regions before dissection from the ventral aspect. (Reproduced with permission from ref. 115.)

would overwhelmingly attenuate 980 nm light, and transform its energy into local heat which could damage cells and tissues. For efficient bioimaging, it is therefore essential to develop a novel lanthanide-based SWIR probe with excitation source optimization. For UCNPs, a solution has already been mentioned above: Nd^{3+}-sensitized UCNPs. The same idea can also be used for DCNPs. In 2014, our group reported a novel kind of β-$NaGdF_4$/Na(Gd,Yb)F_4:Er/$NaYF_4$:Yb/$NaNdF_4$:Yb C/S1/S2/S3 DCNPs as an efficient 800 nm NIR to 1525 nm SWIR probe for *in vivo* bioimaging.[116] C/S1/S2/S3 DCNPs were synthesized using the epitaxial seeded growth method, and are composed of the $NaGdF_4$ core (seed for epitaxial growth), a Na(Gd,Yb)F_4:Er shell (S1, the SWIR-emitting layer), a $NaYF_4$:Yb shell (S2, the energy transfer layer), and a $NaNdF_4$:Yb shell (S3, the energy absorption layer) (Figure 1.10). After absorbing 800 nm excitation energy (Nd^{3+}, $^4I_{9/2} \rightarrow {}^4F_{5/2}$), the S3 transfers its energy into the inner S2 layer ($Nd^{3+} \rightarrow Yb^{3+}$, $^2F_{7/2} \rightarrow {}^2F_{5/2}$). Energy is transferred within this layer by the codoped Yb^{3+} until the Er^{3+} in the S1 is sensitized ($Yb^{3+} \rightarrow Er^{3+}$, $^4I_{15/2} \rightarrow {}^4I_{11/2}$). This results in relaxation from the excited state of Er^{3+} *via* the release of a 1525 nm ($^4I_{13/2} \rightarrow {}^4I_{15/2}$) photon along with phonon vibration.

As the 1525 nm SWIR PL occurs following the resonant transfer of excitation energy from the Yb sensitizer to the Er activator, efficient resonant energy transfer theoretically requires a high concentration of the Yb sensitizer. Therefore, in order to realize the highly efficient 1525 nm SWIR PL, we needed to find an optimal doping concentration for the Yb sensitizer. In our

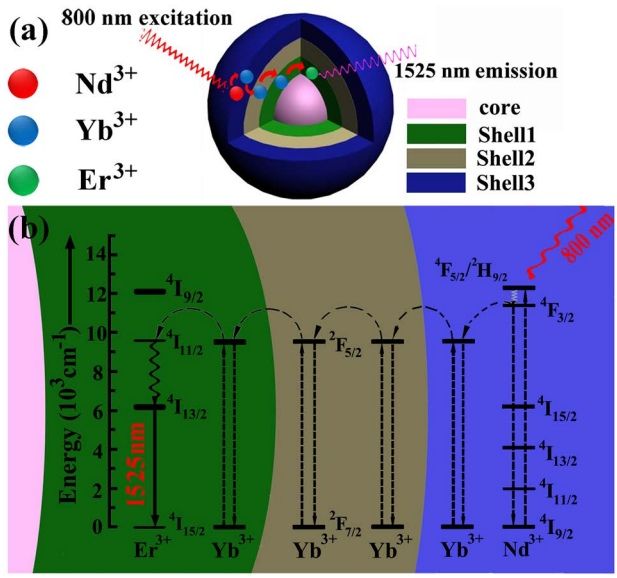

Figure 1.10 (a) Schematic design of the C/S1/S2/S3 DCNPs for 1525 nm luminescence. (b) Proposed energy transfer mechanisms in the multilayer core–shell DCNPs. (Reproduced from ref. 116 with permission from John Wiley and Sons. Copyright © 2014 Wiley-VCH Verlag GmbH & Co. KGaA, Weiheim.)

case, the doping ratio of Yb^{3+} and Er^{3+} can be tuned easily without changing the morphology due to the epitaxial seeded growth method. If we had instead used the $Na(Gd,Yb)F_4$:Er as the starting core of this core–shell nanostructure, the particle size of the $Na(Gd,Yb)F_4$:Er would have been uncontrollable when the Yb : Er doping ratio was changed, resulting in non-comparable spectral data because the PL properties depend on the size of the lanthanide-based NPs. With delicate adjustment of Yb : Er doping ratio, the best composition of the S1 layer was optimized to $NaYbF_4$:2Er to realize the most efficient SWIR emission. Similar experiments were also carried out to optimize the Yb and Nd dopant concentrations in the S2 and S3 layers. We finally found that the optimum composition for efficient 1525 nm SWIR emission under 800 nm excitation is $NaGdF_4$/$NaYbF_4$:2Er/$NaYF_4$:10Yb/$NaNdF_4$:10Yb.

We next studied the penetration depth of our C/S1/S2/S3 NPs. A pellet of the NPs was excited at 800 nm and the 1525 nm signal was imaged using an InGaAs camera through increasing thickness of tissue (pork slices). Notably, SWIR signals from C/S1/S2/S3 NPs were clearly detectable through 1.8 cm of pork tissue, much deeper than the 1.0 cm reported for the 1525 SWIR probe excited by a 980 nm laser under comparable excitation power density (~30 μW), further confirming that the 800 nm excitation source is more suitable for *in vivo* applications. As mentioned above, Moghe *et al.* demonstrated that 1525 nm SWIR transmits more effectively through tissue phantoms than 800 nm NIR light with the same intensity. That was the first experimental demonstration of the imaging advantages of SWIR due to the reduced tissue absorbance and scattering within this second window compared with that of an emitter in the NIR I window. However, there are still no experimental results to evaluate the effect of wavelength on the bioimaging performance around the second NIR window. Here, we systematically evaluated the dependence of *in vitro* and *in vivo* bioimaging performance on the SWIR emission wavelength in comparison to the previously reported $NaGdF_4$:Nd/$NaGdF_4$ NPs with 1060 nm SWIR signal, also upon 800 nm excitation (Figure 1.11a and b). For the 1060 nm wavelength, unlike the 1525 nm wavelength, no signal above background was seen using $NaGdF_4$:Nd/$NaGdF_4$ NPs when the tissue slices were thicker than 1 cm. It is worth mentioning that, in order to accurately compare the penetration depth of 1525 nm and 1060 nm signals, the emitted power of the rare earth pellet and the output power of the NIR source were first matched to have identical spectral intensity before the tissue phantoms were applied.

In addition to good penetration depth, low detection threshold concentration with high resolution is also an essential quality for an optical biomedical imaging agent. As a proof-of-concept experiment, we embedded different concentrations (1, 5, 20, 50, 100 nM) of the amphiphilic 1,2-distearoyl-*sn-glycero*-3-phosphoethanolamine-*N*-[carboxy-(polyethylene glycol)-2000] (DSPE-PEG-2000-COOH) modified C/S1/S2/S3 NPs and $NaGdF_4$:Nd/$NaGdF_4$ NPs into pork muscle tissue at varied depths (5, 8, 15 mm) to investigate the feasibility of bioimaging by a InGaAs camera. It can be seen that the SWIR signals of C/S1/S2/S3 NPs were detectable under 5 mm of pork tissue even when the